

# 7 FEL oscillators and coherent hard x-rays

---

An oscillator FEL is typically a low-gain device that employs an optical cavity to build up and store the field power produced from successive passes through the undulator. Hence, FEL oscillators operate much like traditional lasers based on atomic transitions: radiation is amplified over many passes through the gain medium, which in our case is supplied by the electron beam in the undulator. The first FEL oscillator was demonstrated at Stanford [1] soon after the invention of the FEL concept [2]. Since then, oscillator devices have been built and operated around the world, generating intense radiation in the IR, optical, and UV wavelengths where low-loss, normal-incidence reflectors and accelerators that can produce the required electron beam quality are readily available (see, e.g., [3, 4]).

A hard x-ray free-electron laser in the oscillator configuration – an x-ray FEL oscillator (XFEL) – will produce highly stable x-ray beams of ultra-high spectral purity and high average brightness, offering unique scientific opportunities complementary to those provided by high-gain x-ray amplifiers. The concept for an XFEL using crystals as low-loss reflectors was presented in 1983 [5] at the same workshop where x-ray SASE was first proposed outside of the former Soviet Union [6]. While work in SASE blossomed over the next few decades, the XFEL concept did not receive its due attention until a recent, detailed study showed that an oscillator could be feasible with the low-intensity, ultra-low-emittance electron bunches contemplated for energy recovery linacs [7].

In this chapter we begin by briefly introducing some of the basic operating principles and phenomena that are applicable to a wide range of oscillator FELs. We then discuss many of the physics issues, requirements, and challenges that are unique to an oscillator for x-rays.

## 7.1 FEL oscillator principles

The basic schematic of an FEL oscillator is illustrated in Figure 7.1. Electron bunches from a (usually rf) accelerator pass through an undulator that is located inside a low-loss optical cavity. Starting from an empty cavity, in the first pass the electron beam emits spontaneous undulator radiation that is reflected back into the undulator by the cavity mirrors. In the second pass, the pulse of spontaneous

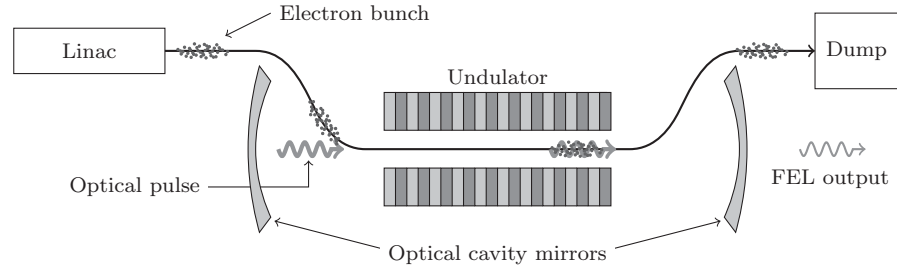


**Figure 7.1** Schematic of an FEL oscillator showing its basic operating principle.

emission meets and overlaps with a second electron bunch at the entrance of the undulator. The radiation and the e-beam interact in the undulator, after which the output field is composed of the spontaneous emission from both the first and second pass, along with an amplified signal due to FEL gain. This process repeats, so that the amplified radiation signal will eventually dominate the output if the gain is larger than the round-trip loss in the cavity.

### 7.1.1 Power evolution and saturation

For a simple mathematical description of the power evolution in an oscillator, let  $P_n$  be the power of the optical pulse at the undulator exit after its  $n^{\text{th}}$  pass, and  $P_s$  be the power of spontaneous emission. Then

$$\begin{aligned} P_1 &= P_s \\ P_n &= R(1 + G)P_{n-1} + P_s \quad \text{for } n \geq 2, \end{aligned} \quad (7.1)$$

where  $G$  is the FEL gain and  $R$  is the reflectivity of the optical transport line. The net single pass power amplification is  $R(1 + G)$ , and evidently the power increases if the single pass gain overcomes the losses such that

$$R(1 + G) > 1. \quad (7.2)$$

This is the “lasing” condition for an FEL oscillator. The power after the  $n^{\text{th}}$  pass is governed by Eqs. (7.1), whose solution is

$$P_n = \frac{[R(1 + G)]^n - 1}{R(1 + G) - 1} P_s. \quad (7.3)$$

Assuming that  $R(1 + G) > 1$ , we see that the power increases exponentially with  $n$  after sufficiently many passes of amplification.

The exponential growth of the intracavity radiation power does not continue indefinitely. Rather, the optical power eventually becomes large enough to trap electrons in the ponderomotive potential and then rotate them to an absorptive phase where they extract energy from the field as we discussed in Sec. 3.3.2. This in turn reduces the gain from its small signal value, and the system reaches a

steady state or “saturates” when the gain decreases to the value  $G_{\text{sat}}$  given by

$$R(1 + G_{\text{sat}}) = 1. \quad (7.4)$$

Furthermore, at saturation the power generated during one pass  $\Delta P$  equals the total losses, so that if the power inside the cavity is  $P_{\text{sat}}$  we have  $\Delta P = (1 - R)P_{\text{sat}}$ . In Sec. 3.3.2 we showed that  $\Delta P \approx P_{\text{beam}}/2N_u$ , which in turn implies that the intracavity radiation power optical power at saturation is

$$P_{\text{sat}} \approx \frac{1}{2N_u(1 - R)} P_{\text{beam}}. \quad (7.5)$$

The optical elements in the cavity, and in particular the mirrors, must be able to withstand the power  $P_{\text{sat}}$  for the oscillator to operate stably.

At saturation the power decreases by an amount  $(1 - R)\Delta P$  during any complete round-trip cycle; this energy loss can be due to many different mechanisms, including radiation absorption in the mirror material, diffraction at the edges of the optical elements, and transmission out of the cavity for useful purposes. If one had an ideal optical line with no losses, the cavity transmission would equal  $(1 - R)$  so that the maximum power that can be coupled out of the oscillator is  $(1 - R)P_{\text{sat}} \approx P_{\text{beam}}/2N_u$ .

Useful output radiation from an FEL oscillator requires it to operate for some time at saturation. Hence, an oscillator can be driven by a pulsed accelerator only if the number of bunches within each macro-pulse is more than that required to reach saturation. With a cw accelerator, on the other hand, the oscillator can be maintained at a steady state indefinitely. This is a desirable mode of operation, since the FEL then provides a stable source with a higher average photon flux.

### 7.1.2 FEL lethargy and gain narrowing

There are many other physics at work in addition to the power evolution just described. One subtle but important phenomenon is lethargy [8] – the fact that the trailing part of the optical pulse (the tail) is more strongly amplified than the front (the head). This is because the initially unmodulated electron beam must propagate some distance through the undulator to develop the density modulation that provides FEL gain, during which time the electron beam and its gain slips behind the field envelope. As a consequence, the bunch spacing does not need to be exactly the same as the round-trip time of the optical pulse to amplify the radiation, and the FEL gain is maximized when the cavity length is slightly shorter than that determined from the round-trip time in the cavity. In fact, FEL oscillators producing IR to UV light typically operate with a cavity length slightly different from the optimum to suppress the synchrotron instability that can amplify perturbations in the field power and lead to an unstable FEL output [9, 10, 11, 12].

The lethargy effect causes the round-trip time of the pulse envelope to be in general different from the round-trip time of the phase, since the latter is

determined essentially by the cavity length. In other words, the phase fronts return to the undulator after a time approximately equal to the round trip time in the cavity (which sets the so-called “synchronism condition”), while the peak of the pulse envelope arrives a time of order the slippage time  $N_u \lambda_1 / c$  after. This fact will be important later when we discuss a nuclear-resonance-stabilized XFEL in section 7.4.

Temporal coherence in an FEL oscillator is achieved by gain narrowing due to the FEL itself and also through spectral filtering provided by the cavity mirrors if their reflectivity is wavelength-dependent. The FEL-induced spectral gain narrowing occurs because the FEL gain is frequency dependent; alternatively, it can be understood as the slow increase in the coherence length from  $N_u \lambda_1$  due to many passes through the undulator. Hence, when the mirror reflectivity is independent of wavelength, we expect that the FEL spectral bandwidth  $\sigma_\omega$  decreases with pass number  $n$  as

$$\left(\frac{\sigma_\omega}{\omega_1}\right)_n \sim \frac{1}{N_u} \frac{1}{\sqrt{n}}. \quad (7.6)$$

For short electron bunches, gain narrowing stops when  $(\sigma_\omega/\omega_1)_n$  becomes the transform limited bandwidth  $\lambda_1/(4\pi\sigma_z)$  associated with the rms length of the electron bunch  $\sigma_z$ . For longer electron bunches that have a current maximum in the center, the non-uniform gain causes the optical pulse profile to also narrow in length/duration, with  $(\Delta z)_n^{\text{rms}} \sim \sigma_z/\sqrt{n}$ . The spectral and temporal narrowing will stop when the pulse is Fourier-transform limited, i.e., at the pass number  $n \sim N_{FT}$  determined by

$$\left(\frac{\sigma_\omega}{\omega_1}\right)_{N_{FT}} (\Delta z)_{N_{FT}}^{\text{rms}} \sim \frac{\lambda_1}{4\pi}, \quad (7.7)$$

from which we determine that the steady state is reached after approximately  $N_{FT} \sim 4\pi\sigma_z/\lambda_1 N_u$  passes, and that the limiting bandwidth is [13]

$$\frac{\sigma_\omega}{\omega_1} \sim \sqrt{\frac{\lambda_1}{4\pi N_u \sigma_z}}. \quad (7.8)$$

This limiting mode is known as the dominant supermode [14]. As we will show, the longitudinal supermodes arise from the dynamic interplay between amplification, gain narrowing, and FEL lethargy.

### 7.1.3 Longitudinal supermodes of the FEL oscillator

In this section we use the simple low-gain model developed by Elleaume [15] to more fully investigate the supermode longitudinal dynamics. This model divides the evolution during a single round trip into its various components: gain that depends on the current and the propagation/slippage in the undulator, reflection by the mirrors, and propagation in the cavity. Assuming that all of these effects result in small perturbations to the radiation (as is true in the low gain regime),

then we can approximate each as acting individually and in succession on the electric field  $E(t)$ . In what follows we discuss these longitudinal effects in turn, and then combine them into a single equation describing the linear dynamics of a low-gain oscillator.

We assume that the FEL gain transforms the field via the amplification operator  $E \rightarrow E + \mathcal{G}[E]$ . To develop a simple model for  $\mathcal{G}$ , we recall that FEL gain depends linearly on the current and that the field interacts with the electron beam within one slippage length  $N_u \lambda_1$ . In terms of the light-cone coordinate  $\tau \equiv z - ct$ , this means that the amplification of  $E(\tau)$  depends on the interaction between the current and field amplitude for points  $\tau'$  satisfying  $\tau \leq \tau' \leq \tau + N_u \lambda_1$  (see, e.g., [16]). We will use a very simple description of this process in which we model the gain operation  $\mathcal{G}[E]$  as increasing the field by an amount depending on the e-beam current and  $E$ -field amplitude at the point one-half the slippage distance  $N_u \lambda_1 / 2$  ahead. Hence, we approximate the amplitude gain from an electron beam with rms length  $\sigma_z$  as acting via

$$\begin{aligned} E(\tau) \rightarrow E(\tau) + \mathcal{G}[E] &\approx E(\tau) + \frac{G}{2} e^{-(\tau + N_u \lambda_1 / 2)^2 / 2\sigma_z^2} E(\tau + \frac{1}{2} N_u \lambda_1) \\ &\approx \left[ 1 + \frac{G}{2} \left( 1 - \frac{\tau^2}{2\sigma_z^2} \right) \right] E(\tau) \\ &\quad + \frac{G}{4} N_u \lambda_1 \frac{\partial E}{\partial \tau} + \frac{G}{16} (N_u \lambda_1)^2 \frac{\partial^2 E}{\partial \tau^2}, \end{aligned} \quad (7.9)$$

where for simplicity we assume that  $\sigma_z \gg N_u \lambda_1$  and that the amplitude gain  $G/2$  is real.<sup>1</sup>

After the FEL interaction, the mirror reduces the field amplitude by the multiplicative factor  $\sqrt{R} \equiv \sqrt{1 - \alpha} \approx 1 - \alpha/2$ , where  $\alpha$  is the (assumed real) power loss. In addition, we include the possibility that the reflectivity depends on frequency by modeling it as a Gaussian filter in  $\omega$  with rms power bandwidth  $\sigma_{\text{refl}}$ . Hence, the mirror results in the transformation

$$\begin{aligned} E(\tau) \rightarrow \int d\omega e^{-i\omega\tau/c} R(\omega) E(\omega) &\approx (1 - \alpha/2) \int d\omega e^{-i\omega\tau/c} e^{-\omega^2/4\sigma_{\text{refl}}^2} E(\omega) \\ &\approx \left( 1 - \frac{\alpha}{2} \right) \int d\omega e^{-i\omega\tau/c} \left[ 1 - \frac{\omega^2}{4\sigma_{\text{refl}}^2} \right] E(\omega) \\ &= \left( 1 - \frac{\alpha}{2} \right) E(\tau) + \frac{c^2}{4\sigma_{\text{refl}}^2} \frac{\partial^2}{\partial \tau^2} E(\tau). \end{aligned} \quad (7.10)$$

Finally, we include the possibility that after one round trip through the cavity the arrival time of the radiation pulse and the next electron bunch may differ by an amount  $\ell/c$ ; this timing difference could be due to adjustments to the cavity length or timing jitter of the electrons, and is modeled by

$$E(\tau) \rightarrow E(\tau + \ell) \approx E(\tau) + \ell \frac{\partial}{\partial \tau} E(\tau). \quad (7.11)$$

<sup>1</sup> The generalization to complex  $G$  and  $\sqrt{R}$  is straightforward but messy. For example, the change in power is  $|1 + G/2|^2 \approx 1 + (G + G^*)/2$  if  $G$  is complex.

A full pass through the oscillator is composed of the transformations (7.9)-(7.11) due to the gain including slippage, the mirror, and the cavity length detuning. Every transformation is written as a sum of the initial field  $E(\tau)$  and a perturbation. If each of these perturbing effects is small, then the field at pass  $(n+1)$  can be written a sum of the various perturbations acting on the field  $E_n$  as follows:

$$E_{n+1}(\tau) \approx E_n(\tau) + \frac{G-\alpha}{2}E_n(\tau) - \frac{G\tau^2}{4\sigma_z^2}E_n(\tau) + \left(\ell + \frac{GN_u\lambda_1}{4}\right)\frac{\partial E_n}{\partial\tau} + \left[\frac{c^2}{4\sigma_{\text{refl}}^2} + \frac{G(N_u\lambda_1)^2}{16}\right]\frac{\partial^2 E_n}{\partial\tau^2}. \quad (7.12)$$

Moving  $E_n$  to the left-hand-side and setting  $E_{n+1} - E_n \approx \partial E_n/\partial n$  leads to a linear partial differential equation for the field  $E_n(\tau)$ . This PDE can be solved by the separation of variables technique, which leads to exponential dependence on  $n$ , while the temporal variation is described by Hermite-Gauss functions. We index these linear modes by  $p$  and find that the general solution can be written as a sum over the ‘‘supermodes’’

$$E_n^p(\tau) = \exp\left[\left(\frac{G-\alpha}{2}\right)n - \left(\frac{2D^2\sigma_{\text{filter}}^2}{c^2} + \frac{c(1+2p)\sqrt{G}}{2\sigma_z\sigma_{\text{filter}}}\right)n\right] \times e^{-2\sigma_{\text{filter}}^2 D\tau/c^2} \exp\left[-\frac{\sqrt{G}c\sigma_{\text{filter}}}{2\sigma_z}\tau^2\right] H_p\left(G^{1/4}\sqrt{\frac{c\sigma_{\text{filter}}}{\sigma_z}}\tau\right), \quad (7.13)$$

where we have defined the net detuning length  $D \equiv \ell + GN_u\lambda_1/4$  and the effective filtering bandwidth  $\sigma_{\text{filter}}$  via

$$\frac{1}{\sigma_{\text{filter}}^2} \equiv \frac{1}{\sigma_{\text{refl}}^2} + \frac{GN_u^2\lambda_1^2}{16}. \quad (7.14)$$

The first line in (7.13) indicates that the exponential power growth is reduced from its nominal value  $G-\alpha$  (gain minus loss) if the total detuning length  $D \neq 0$ ; this condition shows one effect of lethargy since maximum gain is achieved when the cavity length is reduced slightly from its nominal synchronous length (i.e.,  $D = 0$  implies that  $\ell < 0$ ). Significant FEL gain requires the total detuning to be within the effective oscillator bandwidth such that  $D\sigma_{\text{filter}} \ll 1$ . Additionally, setting  $D = 0$  shows that the gain approaches the infinite beam limit only if the electron beam is also significantly longer than the inverse bandwidth  $1/\sigma_{\text{filter}}$ . For shorter electron bunches, only the fraction of current whose spectral content lies within the effective bandpass set by either the mirror  $\sigma_{\text{refl}}$  or the slippage  $4/(N_u\lambda_1\sqrt{G})$  contributes to the gain.

The rms width of the  $p^{\text{th}}$  mode is proportional to the geometric mean of the e-beam size and  $1/\sigma_{\text{filter}}$ , with temporal width  $\sim \sqrt{(1+2p)\sigma_z/c\sigma_{\text{filter}}}$ . When the electron bunch is long there are many longitudinal modes with comparable growth rates, and the oscillator output is comprised of a superposition of supermodes whose total bandwidth  $\sim 1/N_u$  and temporal duration  $\sim \sigma_z$ . As the evolution proceeds through many passes, however, the lowest order ( $p = 0$ )

Gaussian mode with largest gain will eventually become dominant. If the mirror is essentially wavelength independent,  $\sigma_{\text{refl}} \gg 1/N_u \lambda_1$ , our discussion in the beginning of this chapter applies and the output bandwidth will approach the limiting value (7.8), albeit slowly.

On the other hand, we will see that the crystal mirrors that enable FEL oscillators in the x-ray spectral region have  $\sigma_{\text{refl}} \ll 1/N_u \lambda_1$  (typically  $N_u \lesssim 3 \times 10^3$  while  $\sigma_{\text{refl}}/\omega_1 \sim 10^{-5}$  to  $10^{-7}$ ). In this case,  $\sigma_{\text{filter}} \rightarrow \sigma_{\text{refl}}$  which simplifies some of the preceding discussion. For example, the lowest order (Gaussian) supermode simplifies to

$$E_n^0(\tau) = \exp\left[\frac{1}{2}\left(G - R - \frac{4\ell^2\sigma_{\text{refl}}^2}{c^2} - \frac{c\sqrt{G}}{\sigma_z\sigma_{\text{refl}}}\right)n\right] e^{-2\sigma_{\text{refl}}^2\ell\tau/c^2} e^{-\tau^2/2\sigma_0^2}, \quad (7.15)$$

where the mean square temporal width  $\sigma_0^2 \equiv \sigma_z/(\sqrt{G}c\sigma_{\text{refl}})$ . Hence, in this case the gain is reduced from its nominal value if either the cavity length shift  $\ell$  or the electron beam width  $\sigma_z$  is greater than the inverse bandwidth of the mirror  $c/\sigma_{\text{refl}}$ . The steady state temporal width is given by  $\sigma_0 \propto \sqrt{\sigma_z/c\sigma_{\text{refl}}}$  with final bandwidth  $\propto \sqrt{c\sigma_{\text{refl}}/\sigma_z}$ , and it now requires  $N_{FT} \sim 2\sigma_{\text{refl}}\sigma_z/c \ll 4\pi\sigma_z/(\lambda_1 N_u)$  passes to reach this steady state.

In addition to modifying the supermode behavior, the additional spectral filtering provided by the mirrors also completely suppresses the sideband/synchrotron instability, eliminating the unstable and chaotic “spiking mode” of operation observed at lower wavelengths [17, 18]. This is because the sideband instability amplifies frequency content near that associated with the synchrotron period, i.e., with frequencies at  $\omega = \omega_1 \pm \omega_s$ , where

$$\omega_s \sim \frac{\lambda_u}{\lambda_1} ck_s = \frac{\lambda_u}{\lambda_1} \frac{c}{L_u} \sqrt{\epsilon} = \frac{c}{N_u \lambda_1} \sqrt{\epsilon}, \quad (7.16)$$

and we recall that  $\epsilon$  is the normalized field strength defined in (3.25). At saturation  $\epsilon \sim 1$ , so that the characteristic frequency of the sideband/“spiking” mode is

$$\omega_s \sim \frac{c}{N_u \lambda_1} \gg \sigma_{\text{refl}}, \quad (7.17)$$

and the narrow bandwidth of the XFEL crystal mirrors effectively filters out the sideband instability.

#### 7.1.4 Transverse physics of the optical cavity

When the gain is small, the transverse mode is typically well described by the vacuum resonator modes of the cavity. We will briefly describe some of the transverse cavity physics in the limit of Gaussian optics, which assumes that angles from the optical axis are small (paraxial) and that optical elements can be treated as producing linear transformations to the field. In Sec. 1.2.3 we showed that such linear transformations propagate the radiation brightness/Wigner function along rays, which implies that we can analyze the cavity modes using the same matrix formulation that we described for particle beams in Secs. 1.1.2-1.1.4. Under these

limiting circumstances, the transformations act on the (pseudo)distribution of rays in the position-angle phase space  $(\mathbf{x}, \phi)$ , and the wave behavior can be described by referencing only the propagation of rays.<sup>2</sup>

In the laser community the matrix approach is referred to as the ABCD-matrix method [19], and typically these matrix elements are used to derive the stable Rayleigh range and wave front curvature for Hermite-Gaussian cavity modes. The lowest order mode is analogous to a Gaussian particle beam with emittance  $\lambda/4\pi$ , while its Rayleigh length at the waist  $Z_R = \sigma_r^2/(\lambda/4\pi) = (\lambda/4\pi)\sigma_r^2$  is equivalent to the Courant-Snyder beta function from particle optics.

In order to understand the transverse x-ray profile, we first consider the simple two-mirror resonator shown in Fig. 7.2. We model this optical cavity as containing one ideal mirror of focal length  $f$ , such that the round trip distance in the cavity is  $L_c$ . We restrict our discussion to the 2D phase space  $(x, \phi)$ , and recall from Sec. 1.1.4 that the matrices associated with a drift length  $\ell$  and a focusing mirror are, respectively,

$$\mathbf{L}(\ell) = \begin{bmatrix} 1 & \ell \\ 0 & 1 \end{bmatrix} \quad \mathbf{F}(f) = \begin{bmatrix} 1 & 0 \\ -1/f & 1 \end{bmatrix}. \quad (7.18)$$

Stable resonator modes exist when the rms size, divergence, and correlation are periodic over one round-trip through the cavity. These mode sizes can be determined from the the matrix map that starts and ends in the middle of the undulator; for the two-mirror resonator this is given by  $\mathbf{M}_{2\text{res}} = \mathbf{L}(L_c/2)\mathbf{F}(f)\mathbf{L}(L_c/2)$ . The matrix  $\mathbf{M}_{2\text{res}}$  maps  $(x, \phi)$  from and back to the center of the cavity such that

$$\begin{bmatrix} x \\ \phi \end{bmatrix}_{\text{out}} = \mathbf{M}_{1\text{res}} \begin{bmatrix} x \\ \phi \end{bmatrix}_{\text{in}}, \quad (7.19)$$

while the second-order moment matrix  $\Sigma_{\text{out}}$  at the output plane is related to the initial  $\Sigma_{\text{in}}$  via

$$\begin{aligned} \Sigma_{\text{out}} \equiv \begin{bmatrix} \langle x^2 \rangle & \langle x\phi \rangle \\ \langle \phi x \rangle & \langle \phi^2 \rangle \end{bmatrix}_{\text{out}} &= \mathbf{M}_{2\text{res}} \begin{bmatrix} \langle x^2 \rangle & \langle x\phi \rangle \\ \langle \phi x \rangle & \langle \phi^2 \rangle \end{bmatrix}_{\text{in}} \mathbf{M}_{2\text{res}}^T \\ &= \mathbf{M}_{2\text{res}} \Sigma_{\text{in}} \mathbf{M}_{2\text{res}}^T. \end{aligned} \quad (7.20)$$

Equating  $\Sigma_{\text{out}}$  and  $\Sigma_{\text{in}}$  implies that at the cavity middle the correlation vanishes (the radiation has a waist), and that the cavity round trip length  $L_c$  and mirror focal length  $f$  are related to the trapped mode Rayleigh length through the following relation:

$$f = \frac{L_c}{4} + \frac{1}{L_c} \frac{\langle x^2 \rangle_{\text{in}}}{\langle \phi^2 \rangle_{\text{in}}} = \frac{L_c}{4} + \frac{Z_R^2}{L_c}. \quad (7.21)$$

Note that stable operation requires  $f > L_c/4$ , which in terms of the mirror's radius of curvature is  $2f = r > L_c/2$ . This inequality can be violated if there is

<sup>2</sup> Non-ideal elements, apertures, and nonlinear transformations introduce interference effects that may not be well-described by the methods presented here.

sufficient FEL amplification, but for low-gain devices it provides a good starting point for optical cavity design.

In the next section we will describe cavity designs suitable for x-ray FEL oscillators (XFELs). In addition, we will extend the cavity analysis described here to include a more general configuration and tolerance analysis.

## 7.2 X-ray cavity configurations

Like other lasers, FEL oscillators are comprised of two basic components: the gain medium consisting of an undulator and electron beam, and a series of optical elements that trap and focus the radiation to be amplified. Having already explained the essential physical principles behind the XFEL, here we describe how a suitable x-ray optical cavity could be formed. Although no such cavity yet exists, the various optical elements required for an XFEL have been developed over the past few decades, largely due to the demands of synchrotron light sources. For example, the x-ray focusing required for an XFEL cavity can be done with high quality grazing incidence mirrors or with compound refractive lenses (CRLs). However, neither of these focusing elements can work alone: grazing incidence mirrors rely on total external reflection that is appreciable only at very small grazing incidence angles, while CRLs work in transmission. Hence, another optical element that has high reflectivity at near normal angles of incidence is required to efficiently return the radiation to the undulator for amplification. This role can be filled by crystal mirrors based on Bragg reflection from the (nearly) perfectly aligned crystal planes.

X-ray optics based on Bragg reflection work via the coherent scattering of light whose wavelength approximately satisfies the Bragg condition  $\lambda = 2a \sin \Theta$ , where  $\Theta$  is the angle from grazing incidence and  $a$  is the atomic spacing between the crystalline planes. The spectral width of large reflectivity, called the Darwin width, is inversely proportional to the number of crystal planes that contribute to the reflection. For hard x-rays more than  $10^5$  crystal planes may contribute, so that typically  $\sigma_{\text{refl}}/\omega_1 \lesssim 10^{-5}$  at 5 keV and  $\sigma_{\text{refl}}/\omega_1 \lesssim 10^{-7}$  at 20 keV. Within the Darwin width the reflectivity can approach 100%, meaning that Bragg crystals may enable a low-loss optical cavity for x-rays that efficiently filters the FEL output.

The simplest cavity configuration is illustrated in Figure 7.2, which uses two Bragg crystals to trap the x-rays and a single grazing incidence mirror to shape and focus the transverse mode. This cavity is a realization of the two-mirror resonator described previously. In order to have a large reflectivity, the grazing angle of incidence at the curved mirror must be less than the critical angle of total external reflection, which is typically a few mrad. The radiation in turn must be approximately normal to the Bragg crystal,  $\Theta = \pi/2$  within a few mrad; converting this angular extent into a wavelength range using Bragg's law

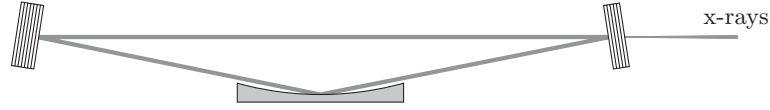


**Figure 7.2** A basic, two-crystal scheme for an XFEL optical cavity that is not tunable. Here, the focusing is provided by a grazing incidence mirror, although other options are possible. Adapted from Ref. [20].

$\lambda = 2a \sin \Theta$  implies that the two-crystal cavity supports FEL lasing over a severely limited spectral/tuning range.

### 7.2.1 Four crystal, wavelength tunable XFEL cavity

Tunable XFELs require cavities with more than two Bragg crystals, and we show an example of a four-crystal configuration in Figure 7.3. This particular design wraps up the four-bounce monochromator invented by Cotterill [21] into a closed, bow-tie shaped cavity. The wavelength can be changed by adjusting the four crystals' Bragg angles in unison while keeping a constant round-trip path length by a coordinated translation of the crystals. The four-crystal scheme also allows one to use a single crystal material (with different reflection planes) over the entire 5-20 keV spectral range of the XFEL. This is an important advantage, since XFELs operating at any wavelength can then employ diamond crystals which, as we will discuss shortly, have excellent thermo-mechanical properties.

To study the four-crystal cavity of Fig. 7.3(a), we assume that the role of the crystals is solely to deflect the ray, in which case this configuration is equivalent to the linear periodic system shown in Fig. 7.3(b). We take the focusing elements  $F_1$  and  $F_2$  to have focal length  $f$ , and label the relevant cavity distances as shown. Note that  $W_1$  is the position of the waist at the middle of the undulator, while the other waist is located at  $W_2$ . Using the same notation for the free space and focusing transport matrices as in Eq. (7.18), one period through the cavity is given by

$$M_{4cr} = L(\ell_1) F(f) L(2\ell_2) F(f) L(\ell_1). \quad (7.22)$$

Stability requires that  $|\text{Tr}(M)| < 2$ , which can be shown to be equivalent to  $f > 0$  and

$$0 < \left( \frac{\ell_1}{f} - 1 \right) \left( \frac{\ell_2}{f} - 1 \right) < 1. \quad (7.23)$$

Consequently, a stable cavity either has both  $\ell_{1,2} > f$  or  $\ell_{1,2} < f$ . If we assume that this four-crystal cavity reduces to the two-mirror cavity discussed previously in the limit  $\ell_2 \rightarrow \ell_1 = L_c/2$ , then we can show that the FEL oscillator has drift half-lengths  $\ell_{1,2}$  that are longer than the focal length  $f$ . To do this we use the stability condition Eq. (7.21) to find that  $f = (\ell_1/2)(1 + Z_R^2/\ell_1^2)$ , and recall that FEL gain is maximized when  $Z_R \sim L_u/2\pi$ , so that  $Z_R^2/\ell_1 < 1$  and  $\ell_1 > f$ .

As we just mentioned, the Rayleigh range inside the undulator  $Z_{R,1}$  is chosen

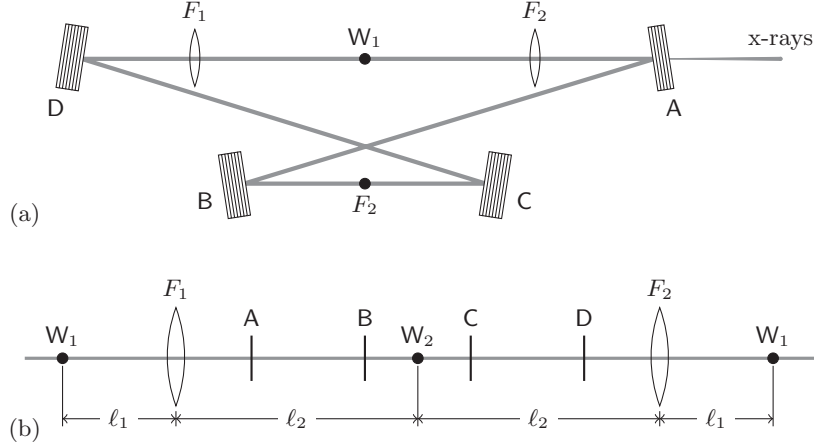


**Figure 7.3** (a) A diagram of a tunable cavity configuration using four crystals. The focusing elements  $F_1$  and  $F_2$  could represent grazing incidence mirrors or compound refractive lenses (CRLs). (b) Unfolded optical lattice equivalent to the 4-crystal cavity. A, B, C, and D label the crystal positions, while  $W_1$  ( $W_2$ ) indicate the position of the radiation waist inside (outside) the undulator. Adapted from Ref. [20].

so as to maximize the FEL gain. On the other hand, there is considerably more freedom in selecting  $Z_{R,2}$ , which, as shown in Fig. 7.3, governs the divergence of the radiation seen by the crystal mirrors. Since the Bragg crystal angular acceptance is related to the bandwidth of large reflectivity through Bragg's law  $\lambda = 2a \sin \Theta$ , we see that it is advantageous to decrease the radiation divergence at the crystal by increasing  $Z_{R,2}$ . To determine the stable Rayleigh lengths, we equate the second order moment matrices via  $\Sigma_{\text{out}} = M_{4\text{cr}} \Sigma_{\text{in}} M_{4\text{cr}}^T$ , to find that

$$Z_{R,1} = \sqrt{\frac{\ell_1 - f}{\ell_2 - f} [f(\ell_1 + \ell_2) - \ell_1 \ell_2]^{1/2}} \quad Z_{R,2} = \frac{\ell_2 - f}{\ell_1 - f} Z_{R,1}. \quad (7.24)$$

Hence, we can extend the Rayleigh range  $Z_{R,2}$  and decrease the x-ray divergence on the crystals by making the length  $\ell_2$  longer than  $\ell_1$ .

We can determine the tolerance in the orientation of the crystals by using a standard method from accelerator physics. Suppose the crystal A is oriented at an angle  $\Delta\Theta$  from the ideal angle, so that an on-axis ray is deflected by an angle  $2\Delta\Theta$ . The coordinates of the displaced optical axis at  $W_1$  can be found by requiring that the displaced reference trajectory is periodic with the period of the optical system:

$$\begin{bmatrix} \Delta x \\ \Delta \phi \end{bmatrix} = M_{4\text{cr}} \begin{bmatrix} \Delta x \\ \Delta \phi \end{bmatrix} + L(\ell_1) F(f) L(2\ell_2 - d_A) \begin{bmatrix} 0 \\ 2\Delta\Theta \end{bmatrix}, \quad (7.25)$$

where  $d_A$  is the distance from  $F_1$  to crystal A. The first term in Eq. (7.25) is the round-trip transformation from the waist  $W_1$  at the undulator center, while the second includes the angular deviation due to an error at crystal A.

Solving (7.25) will give the displaced ray position  $\Delta x$  and angle  $\Delta\phi$  as a function of the angular error  $\Delta\Theta$ . The tolerance is set by requiring the resulting ray displacements in position and angle to be much less than mode size and angular divergence,  $|\Delta x| \ll \sigma_r$  and  $|\Delta\phi| \ll \sigma_{r'}$ . For typical XFEL parameters  $\sigma_r \approx 10 \mu\text{m}$  and  $\sigma_{r'} \approx 1 \mu\text{rad}$ , and the resulting angular tolerance  $\Delta\Theta \lesssim 10 \text{ nrad}$ . It appears that the null-detection feedback technique employed at the Laser Interferometer Gravitational-Wave Observatory (LIGO) may be able to achieve this high level of stability for multiple optical axes with a single detector, and therefore appears to be a promising stabilization approach.

Finally, preserving the wavefronts through the optical cavity place additional tolerances on the smoothness of the optical elements. For diamond crystals, the surface error height  $\delta h$  should be a fraction of the x-ray wavelength times the difference of the index of refraction from unity. Since for hard x-rays the refractive index differs from one by an amount of order  $10^{-6}$ , the tolerance on  $\delta h$  is about a micron, which should be achievable; similar considerations for CRLs give a similar constraint on its surface. On the other hand, the surface requirements of the grazing incidence mirror can be divided up into a height error, which contributes to diffuse scattering and an effective reduction in reflectivity, and figure error, which contributes to mode distortion. The requirement on the height error for a grazing incidence mirror is about 1 nm, while the latter figure error is about  $0.1 \mu\text{rad}$ ; both tolerances are demanding but within the current state of the art.

### 7.2.2 Diamond crystals for XFEL

Diamond is a material whose superb physical qualities are well suited to an XFEL cavity: high mechanical hardness, high thermal conductivity, high radiation hardness, low thermal expansion, and chemical inertness. An exceptionally high  $\geq 99\%$  reflectivity is predicted in x-ray Bragg diffraction, higher than that from any other crystal. This is because the distance over which x-rays are reflected from diamond (the so-called “extinction length”) is much shorter than the characteristic absorption length; in other words, diamond has a uniquely small ratio of the extinction length to the absorption length that leads to a near perfect reflectivity. Hence, the primary source of loss come from imperfections and impurities in the crystal structure. Recent developments in the manufacture of synthetic diamond crystals have shown that nearly defect-free crystals of suitable size for an XFEL can be produced, while experiments with 13.9-keV and 23.7-keV x-ray photons have established that the predicted reflectivity greater than 99% at near normal incidence can be achieved [22].

In addition to its large reflectivity, diamond is also well-suited to handle the thermal heat load from an XFEL. Specifically, since Bragg crystals rely on the periodic lattice spacing, one must determine if temperature gradients from radiation heating could lead to strain in the material and gradients in the lattice spacing. Fortunately, diamond has a very large thermal diffusivity and an

extremely small coefficient of thermal expansion for  $T < 100$  K, so that the expansion of cryogenically cooled diamond crystals due to heating can be neglected.

### 7.3 XFEL parameters and performance

The major parameters of an example XFEL system from reference [20] are listed in Table 7.1. The electron beam parameters considered here are relatively conservative. XFEL parameters with higher beam qualities, lower bunch charge, and lower electron beam energy may also be feasible [23]. Operating an XFEL with Bragg reflectors will be difficult below 5 keV due to enhanced photo-absorption in the crystal at low photon energies, and limited to a maximum photon energy of around 20 keV because of the decreasing crystal bandwidth at high energy. Although in principle the four-crystal configuration can be adjusted over a very wide range of wavelengths, the practical tuning range for a specific Bragg plane is limited to 2-6% because the angular acceptance can become smaller than the x-ray beam divergence at lower Bragg angles. We note that a few percent is in fact a huge tuning range in comparison to the very narrow bandwidth of  $\sim 10^{-7}$ .

The profiles of the radiation output near the energy of 14.4 keV are shown in Figure 7.4 [20]. In panel (a) the output radiation power as a function of time is indicated as the solid line, with the electron beam current envelope as a dashed line for reference. In panel (b) we plot the corresponding output spectrum with a solid line, showing that the spectral FWHM is approximately 1.8 meV, corresponding to a relative FWHM of  $\sim 1.3 \times 10^{-7}$ . Note that this bandwidth is much narrower than the reflectivity width of the Bragg crystals (the dashed line), and instead approximately equals  $c/\sigma_z$ . This is because after saturation the radiation envelope follows that of the electron beam current, so that radiation spectral profile is roughly given by the Fourier transform of the electron current profile. These steady state pulses are reached after  $\sim 1000$  passes.

### 7.4 X-ray frequency combs from a mode-locked FEL oscillator

The output of an FEL oscillator is a train of radiation pulses, each of which is essentially a copy of the single trapped pulse that is circulating in the cavity. Hence, if the cavity and accelerator are sufficiently stable, the radiation coherence can be extended across multiple pulses, in which case the output spectrum becomes a comb of narrow spectral lines. This is the same basic physics at play in frequency stabilized mode locked lasers (see, e.g., [24]).

To understand how these spectral lines emerge, consider the electric field of

**Table 7.1** Major XFELO parameters.

Electron Beam	
Energy	5-7 GeV
Bunch charge	25-50 pC
Bunch length (rms)	0.1-1 ps
Normalized rms emittance	$\leq 0.2\text{-}0.3$ mm-mrad
Energy spread (rms)	$\lesssim 2 \times 10^{-4}$
Bunch repetition rate	$\sim 1$ MHz (constant)
Undulator	
Period length	$\sim 2$ cm
Deflection parameter $K$	1.0-1.5
Length	30-60 m
Optical Cavity	
Configuration	2-4 diamond crystals + focusing mirrors
Total roundtrip reflectivity	$> 85\%$ (50% for 100-A peak current)
Total length	$\sim 100$ m
XFELO Output	
Photon energy coverage	5-25 keV (plus the third harmonic)
Spectral purity	1-10 meV ( $10^{-6}\text{-}10^{-7}$ in relative BW)
Coherence	Full transverse and temporal coherence
X-ray pulse length	0.1-1.0 ps
Tuning range	2-6 %
Number of photons/pulse	$\sim 10^9$
Pulse repetition rate	$\sim 1$ MHz
Peak spectral brightness	$10^{32}\text{-}10^{34}$ ph/[s $\cdot$ mm $^2$ $\cdot$ mrad $^2$ (0.1% BW)]
Average spectral brightness	$10^{26}\text{-}10^{28}$ ph/[s $\cdot$ mm $^2$ $\cdot$ mrad $^2$ (0.1% BW)]

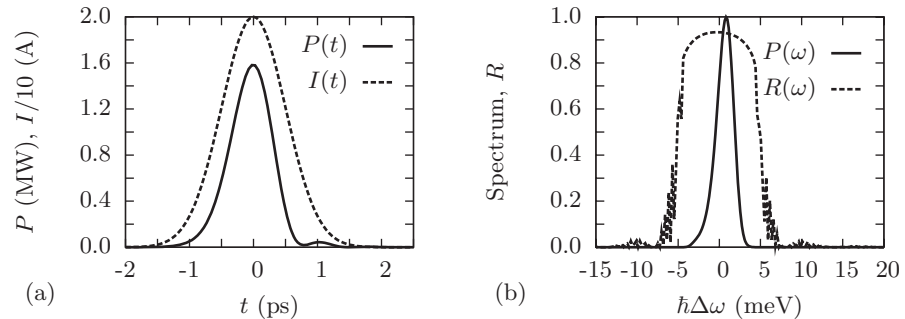


**Figure 7.4** (a) The solid line plots the temporal power profile of the XFELO output at 14.4 keV, showing peak powers  $\sim 1.5$  MW; the electron beam current with  $\sigma_t = 0.5$  ps is shown as a dashed line. (b) Spectrum of the same XFELO output as a solid line. The FWHM bandwidth of  $\sim 2.4$  meV is narrower than that of the crystal reflectivity, shown as the dashed line. Adapted from Ref. [20].

the pulse train,

$$E(t) = \sum_n e^{-i\omega_{\text{FEL}}(t-nT_c)} A(t-nT_e). \quad (7.26)$$

Here  $A(t)$  is the radiation envelope,  $\omega_{\text{FEL}} \approx \omega_1$  is the FEL frequency in the middle of its bandwidth,  $T_c$  is the round-trip time of the EM field in the cavity, and  $T_e$  is the electron bunch spacing. The above equation is in accord with the discussion in section 7.1.2, namely, that the phase advance per period is  $T_c$  while the envelope advance per period is  $T_e$  (we are neglecting here the small index of refraction during the FEL interaction). Fourier transforming to obtain the spectrum, we find that

$$|\tilde{E}(\omega)|^2 = |\tilde{A}(\omega - \omega_{\text{FEL}})|^2 \frac{\sin^2\{N[(\omega - \omega_{\text{FEL}})T_e + \omega_{\text{FEL}}T_c]\}}{\sin^2[(\omega - \omega_{\text{FEL}})T_e + \omega_{\text{FEL}}T_c]}. \quad (7.27)$$

First, note that the overall spectral shape is determined by the single pulse envelope  $\tilde{A}(\omega)$ , so that the total extent in frequency will be of order the e-beam bandwidth  $\sim c/\sigma_z$ . Within this envelope are a sequence of evenly spaced spectral lines that comprise the frequency comb; the frequency location of each “tooth” of the comb is given when the denominator vanishes, namely, at the frequencies

$$\omega_m = \omega_{\text{FEL}} + \frac{\pi}{T_e} \left( m - \frac{\omega_{\text{FEL}}T_c}{\pi} \right) \quad (7.28)$$

for integer  $m$ . Hence, the line spacing is inversely proportional to the time between electron bunches,  $\Delta\omega_{\text{line}} = \pi/T_e$ . Since the frequency comb extends over the envelope bandwidth  $\sim c/\sigma_z$ , there are of order  $cT_e/\sigma_z$  comb lines. Additionally, the numerator of (7.27) implies that the width of each line scales inversely with the number of pulses in the train, so that each line’s bandwidth  $\sim \Delta\omega_{\text{line}}/N = \pi/NT_e$ .

The previous discussion assumes that the cavity is perfectly stable, so that both the bunch spacing  $T_e$  and round-trip time in the cavity  $T_c$  are precisely fixed. If these times fluctuate or otherwise vary, however, the comb lines can be effectively broadened to the point where their width exceeds the spacing  $\Delta\omega_{\text{line}}$ . In this case the comb structure vanishes and the coherence between different pulses is lost. Looking at the formula for the pulse train (7.26), we see that the cavity round-trip time  $T_c$  appears in the phase, while the dependence on bunch spacing  $T_e$  is in the field amplitude. Since the comb spectrum relies on careful phase cancellation, we expect that  $T_c$  must be held constant to a fraction of a wavelength, while the tolerance associated with  $T_e$  will be significantly more relaxed.

To show how variations in  $T_c$  and  $T_e$  affect the comb structure, we first write the product  $\omega_{\text{FEL}}T_c/\pi$  in terms of its integer and fractional part, so that the cavity time is

$$T_c = \frac{\pi M}{\omega_{\text{FEL}}} + t_c, \quad (7.29)$$

with the integer  $M$  chosen such that  $0 \leq \omega_{\text{FEL}} t_c / \pi < 1$ . Then, setting  $m - M \rightarrow m$  in Eq. (7.28), we see that the comb lines are located at

$$\omega_m = \omega_{\text{FEL}} + \frac{\pi}{T_e} \left( m - \frac{\omega_{\text{FEL}} t_c}{\pi} \right). \quad (7.30)$$

The comb lines will persist provided the fluctuations in the fractional cavity time  $t_c$  and the bunch spacing  $T_e$  move  $\omega_m$  a small part of the distance between the spectral lines  $\Delta\omega_{\text{line}} = \pi/T_e$ . If we first consider variations in the electron bunch spacing  $\delta T_e$ , we find that

$$|\delta T_e| \ll \left| \frac{T_e}{m - \omega_{\text{FEL}} t_c / \pi} \right| \lesssim \frac{\sigma_z}{c}, \quad (7.31)$$

where we have used the fact that there are of order  $cT_e/\sigma_z$  comb lines. Variations in the bunch spacing must therefore be much less than the e-beam width, a requirement that we previously found must be met by any oscillator in order to preserve FEL gain. Note that the radiation wavelength does not enter the requirement here, which is a consequence of the dependence on the bunch spacing  $T_e$  appearing in the field amplitude.

On the other hand, requiring that variations in the cavity round-trip time  $\delta T_c$  do not adversely affect the comb leads to

$$|c\delta T_c| \ll \frac{c\pi}{\omega_{\text{FEL}}} \approx \frac{\lambda_1}{2}, \quad (7.32)$$

so that the cavity length must be held constant to within a fraction of the FEL wavelength. This can lead to very strict requirements on the stability of the cavity length, which is a consequence of the fact that  $T_c$  dictates the radiation phase from pass to pass.

Stabilizing the cavity length to a fraction of a wavelength requires an extremely sensitive feedback system capable of measuring and correcting tiny errors. This is particularly true at x-ray wavelengths, where fluctuations must be less than the diameter of an atom. Although very stringent, the desired XFEL stabilization appears to be feasible by a feedback system referenced by, for example, the  $^{57}\text{Fe}$  nuclear resonance [25], since the resonance width and the comb spacing is comparable ( $\sim 10$  neV). The feedback principle is illustrated in Figure 7.5 and works as follows. The comb line moves one comb spacing if the cavity length changes by one FEL wavelength. With one of the comb lines overlapping with the  $^{57}\text{Fe}$  resonance well inside the FEL bandwidth, the cavity length is scanned by one wavelength ( $\sim 0.8$  Å) and held fixed where the fluorescence signal is maximum. Note that it is not necessary to identify which comb line overlaps with the nuclear resonance. It is only necessary that one of the lines does overlap, and we are keeping that line at that position.

Realizing such a nuclear resonance stabilized XFEL (NRS-XFEL) appears to be within the current state of the art, at least with  $^{57}\text{Fe}$  resonance. Extending the stabilization to narrower resonances by an order of magnitude may also be feasible. NRS-XFELs for even narrower resonances will be quite challenging

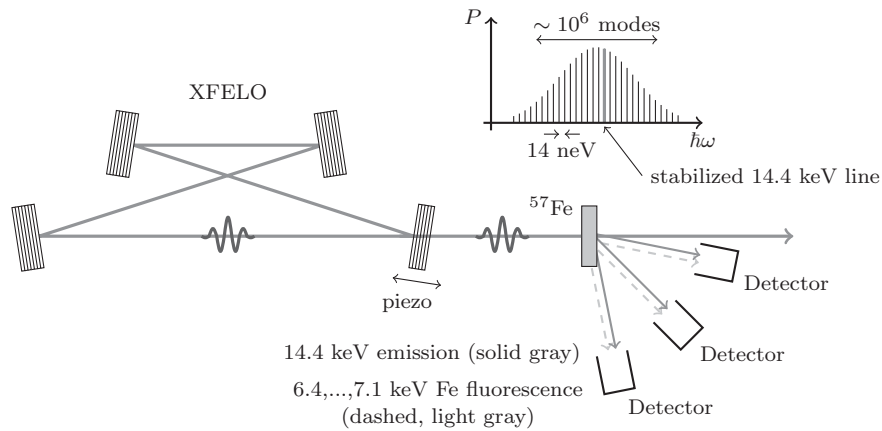


**Figure 7.5** Schematic of the cavity-stabilization scheme. A nuclear-resonant sample (here  $^{57}\text{Fe}$ ) is placed into the XFELO output, and the nuclear-resonant and K-shell electronic fluorescence are monitored as functions of cavity tuning with a piezoelectric actuator. A feedback loop keeps one of the ca.  $10^6$  longitudinal modes of the XFELO on resonance with the sample. Adapted from Ref. [25].

but worthwhile as they provide new scientific techniques hitherto not available in hard x-ray wavelengths.